ROSAT AND ASCA OBSERVATIONS OF THE CRAB-LIKE SUPERNOVA REMNANT N157B IN THE LARGE MAGELLANIC CLOUD

Q. Daniel Wang

Dearborn Observatory, Northwestern University, 2131 Sheridan Road, Evanston, IL 60208-2900; wqd@nwu.edu

AND

Eric V. Gotthelf

NASA/Goddard Space Flight Center, Greenbelt, MD 20771; gotthelf@gsfc.nasa.gov

ABSTRACT

We report the results of *ROSAT* and *ASCA* X-ray observations of the supernova remnant N157B (or 30 Dor B, SNR 0539−69.1) in the Large Magellanic Cloud. For comparison, we also briefly describe the results on SNR 0540−69.3, the only confirmed Crab-like remnant in the Cloud. The X-ray emission from N157B can be decomposed into a bright comet-shaped feature, superposed on a diffuse emission region with a dimension of ∼20 pc. The flat and *nearly* featureless spectrum of the remnant is distinctly different from those of young shell-like remnants, suggesting a predominantly Crab-like nature of N157B. Characterized by a power law with an energy slope of ∼1.5, the spectrum of N157B above ∼2 keV is, however, considerably steeper than that of SNR 0540−69.3, which has a slope of ∼1.0. At lower energies, the spectrum of N157B presents marginal evidence for emission lines, which if real most likely arise in hot gas of the diffuse emission region. The hot gas has a characteristic thermal temperature of 0.4–0.7 keV. No significant periodic signal is detected from N157B in the period range of 3×10^{-3}–2000 s. The pulsed fraction is $\lesssim 9\%$ (99% confidence) in the 2–7 keV range.

We discuss the nature of the individual X-ray components. In particular, we suggest that the synchrotron radiation of relativistic particles from a fast-moving ($\sim 10^3$ km s^{-1}) pulsar explains the size, morphology, spectrum, and energetics of the comet-shaped X-ray feature. We infer the age of the remnant as $\sim 5 \times 10^3$ yr. The lack of radio polarization of the remnant may be due to Faraday dispersion by foreground H II gas.

Subject headings: ISM: individual (N157B) — Magellanic Clouds — supernova remnants — X-rays: ISM

1. INTRODUCTION

Only three supernova remnants (SNRs) have been unambiguously confirmed to be Crab-like: SNR 0540−69.3, MSH 15−52, and the Crab Nebula itself. These remnants show centrally peaked morphologies and flat emission spectra; the emission comes predominantly from synchrotron nebulae powered by embedded young pulsars. There are a number of SNRs that have similar morphologies and spectral characteristics but contain no detected pulsars. N157B is such a remnant (Mills, Turtle, & Watkinson 1978; Clark et al. 1982; Mathewson et al. 1983; Wang & Helfand 1991; Chu et al. 1992, hereafter CKSL92; Dickel et al. 1994, hereafter D94). Like SNR 0540−69.3, N157B is in the Large Magellanic Cloud (LMC) and thus has a good distance determination. But, previous observations have shown no clear correspondence between the morphologies of N157B in the radio, optical, and X-ray regions. The remnant's age of $\sim 2.4 \times 10^4$ yr, inferred from kinematics of optical features (CKSL92), is also much greater (by a factor of about 10) than the confirmed Crab-like SNRs. No radio polarized emission has been detected from N157B, as might be expected for a synchrotron nebula (D94). In short, the exact nature of the remnant has been uncertain.

Here we report new results on N157B, based primarily on observations from the *ROSAT* and *ASCA* X-Ray Observatories. These observations provide much improved timing, imaging, and spectral resolution capabilities. For comparison, we also present the results of analyzing a 40 ks *ASCA* observation on SNR 0540−69.3. We describe the reduction of the X-ray observations in § 2 and present our analysis and results in § 3. Then in § 4, we discuss the implications of our results, together with previous observations, and postulate scenarios to explain various components of N157B. We summarize our results and conclusions in § 5. Appendix A describes an algorithm we used for extracting *ASCA* spectra with correction for the instrument point-spread function (PSF). Throughout the paper, we adopt an LMC distance of $D \approx 47$ kpc (Gould 1995), at which 1′ corresponds to 14 pc.

2. OBSERVATIONS AND DATA REDUCTION

2.1. *ASCA Observations*

Table 1 summarizes parameters of the two *ASCA* observations used in this study. Both observations were acquired during *ASCA*'s Performance Verification phase, and the data were made available through the public archive. Since the *ASCA* has two types of instruments, which observe simultaneously—a pair of Solid-State Imaging Spectrometers (SIS) and a pair of Gas Imaging Spectrometers (GIS)—the two *ASCA* observations yielded eight sets of data: four from the SISs and four from the GISs. The SIS has an energy coverage approximately in the 0.5–8 keV range and the GIS in the 0.8–10 keV range (Tanaka, Inoue, & Holt 1994).

Data from the SIS detectors were collected in 4-CCD FAINT and BRIGHT modes. The data were processed by converting the FAINT mode data to BRIGHT mode equiv-

TABLE 1

SUMMARY OF *ASCA* EXPOSURES ON N157B

Detector (CCD Chip)	Exposure Time (s)	Source Counts[a]	Off-Axis Distance (arcmin)	Vignetting Fraction
ASCA Sequence No. 20000000				
SIS0 (C2)............	16743	2961	3.06	0.90
SIS1 (C0)............	19245	2717	7.17	0.64
GIS2	30820	6784	3.43	0.87
GIS3	30816	5856	7.14	0.64
ASCA Sequence No. 50002000				
SIS0 (C0+C3)......	26123	2758	8.97	0.54
SIS1 (C2+C1)......	16876	2623	4.01	0.84
GIS2	30543	5727	7.24	0.64
GIS3	30538	6171	7.12	0.64

[a] SIS and GIS counts are obtained within $1\farcm7$ and $4\farcm0$ radius circles centered on N157B.

alent data and by filtering the combined set through the standard cleaning criteria. CCD pixels with anomalous counts were identified and excluded using the CLEANSIS technique (Gotthelf 1993). Detailed procedures of these methods can be found in Day et al. (1995). Figure 1 presents an exposure corrected, smoothed SIS image of the 30 Dor region created by combining screened data from both observations.

The SIS data are the most useful in our spectral study of N157B, because of both the broadband energy coverage and the good spectral resolution $[\delta E/E \sim 0.02(5.9 \text{ keV}/E)^{0.5}]$. The spatial resolution of the data is, however, limited by the poor PSF of the *ASCA* telescope. Although the PSF has a sharp core with a FWHM of $\sim 1'$, the broad wing of the PSF produces a 50% encircled radius of $\sim 1\farcm5$ (Jalota, Gotthelf, & Zoonematkermani 1992). The PSF also contains some energy dependence that is most notable above ~ 6 keV. The broad wing of the PSF prevents an *independent* measurement of the background in the region of the source uncontaminated by the source spectrum itself.

We thus devised a method that simultaneously solves for both the source and background spectra (see Appendix A for details). We applied this method to determine the *ASCA* spectra for both N157B and SNR 0540−69.3. To minimize the uncertainties in the spectral background subtraction, we chose a small on-source aperture of radius $1\farcm7$ and a concentric background annulus with its inner and outer radii of $2\farcm3$ and $4\farcm9$. We further used only the southwest half of the background annulus around N157B to avoid the possible contamination by the 30 Dor nebula in the northeastern half of the annulus. Within the on-source aperture of this remnant, the background accounts for about 7% of the total observed intensity with a relatively soft spectrum. Judging from the background intensity variation around N157B, the uncertainty in the background should be less than $\sim 50\%$. This uncertainty in the background subtraction is probably within the systematic error of the data and the analysis.

For each SIS data set of N157B we generated an appropriate background spectral file to match the on-source file. These spectra were then summed for both CCD detectors and for both observations. Individual response files were summed to create an appropriate count-weighted multi-CCD detector and multitelescope response matrix. The summation was accomplished using the FTOOL MATHPHA to add *ASCA* spectral files, and the combined

instrument/response files were merged using the FTOOL ADDRMF.[1] The spectra were binned to contain at least 25 counts for χ^2 model fits. Our final spectral analysis of N157B was based on this summed spectrum and response. We also conducted fits to the four sets of spectra before the summation and found that the results were consistent with those from fits to the summed spectrum, which was certainly much easier to analyze and made multicomponent model fits possible.

The GIS data are the most suitable for timing analysis to search for a putative pulsar in N157B. All the GIS data, acquired in the highest PH time resolution mode (10 bit), sets a limit on the timing accuracy during spacecraft telemetry downlinks of 0.3 ms for HIGH bit rate. However, the calibration of the absolute time (ASCATIME) is only considered accurate to about 2.0 ms (Hirayama et al. 1996). A pulsar search that combined high and medium bit-rate mode data limits the overall accuracy to 5 ms; low bit-rate mode data were excluded from our pulsar search. We converted the arrival time of each count to the barycentric dynamical time, using the FTOOL task TIMECONV. We also extracted a GIS light curve from the *ASCA* observation of PSR 0540−69.3 to be used as a control on our procedure.

The SIS data are of limited use in timing analysis. The 4-CCD mode SIS observation of N157B used a 16 s integration (time between CCD readout), setting a fundamental limit on searches for frequencies faster than 0.03125 Hz, the appropriate Nyquist frequency.

2.2. *ROSAT Observations*

We utilized two *ROSAT* observations from the *ROSAT* High Resolution Imager (RHRI) and one from the *ROSAT* Positional Sensitive Proportional Counter (PSPC). Both the PSPC and RHRI were sensitive to photons in the $\sim 0.1–2$ keV range.

The RHRI observations with a PSF of $\sim 6''$ (FWHM) are the best for studying the spatial properties of N157B. One of the RHRI observations (*ROSAT* Sequence No. rh600228) with an effective exposure of 30094 s was pointed at R136, $\sim 7'$ away from N157B; the other (wh500036) of 4460 s was pointed directly at N157B. Each RHRI observation covers a field of $\sim 34'$ diameter. A co-added intensity

---

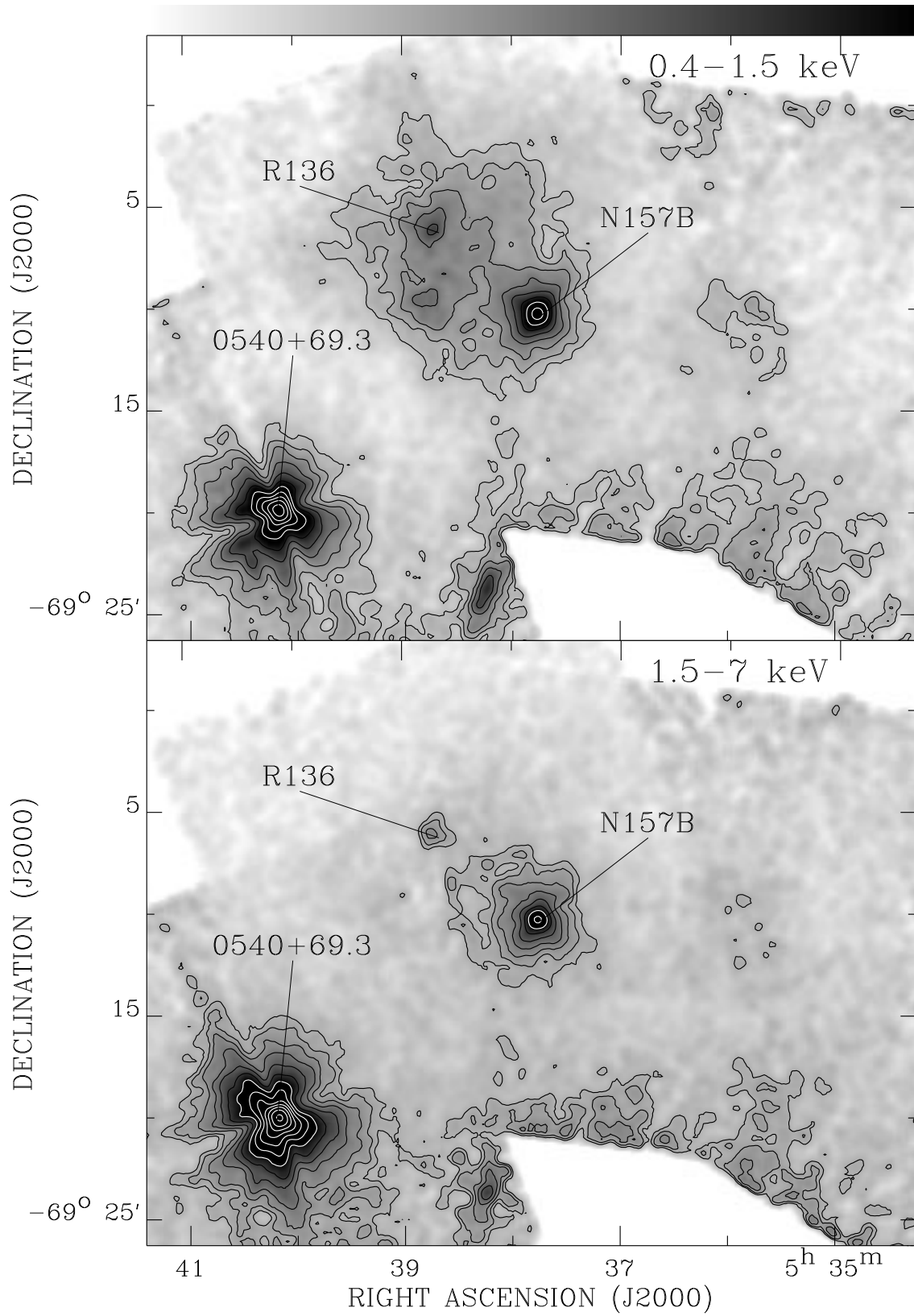[1] Information of the FTOOLS software package is available in the *ASCA* data analysis guide (Day et al. 1995).

FIG. 1.—*ASCA* SIS maps of the 30 Dor region. The maps are corrected for exposure and vignetting. The contours are at (3.0, 4.0, 5.5, 7.8, 11, 16, 24, 35, 52, 77, and 116) × 10^{-3} counts s^{-1} arcmin^{-2} in the 0.4–1.5 keV band, and at (1.7, 2.3, 3.2, 4.6, 6.6, 9.6, 14, 21, 31, 47, 69, 104, and 156) × 10^{-3} counts s^{-1} arcmin^{-2} in the 1.5–7 keV band. Faint radial strips near the southeastern boundaries of the map, especially in the 1.5–7 keV band, are due to stray light (reflected mirror rays) from LMC X-1 to the south.
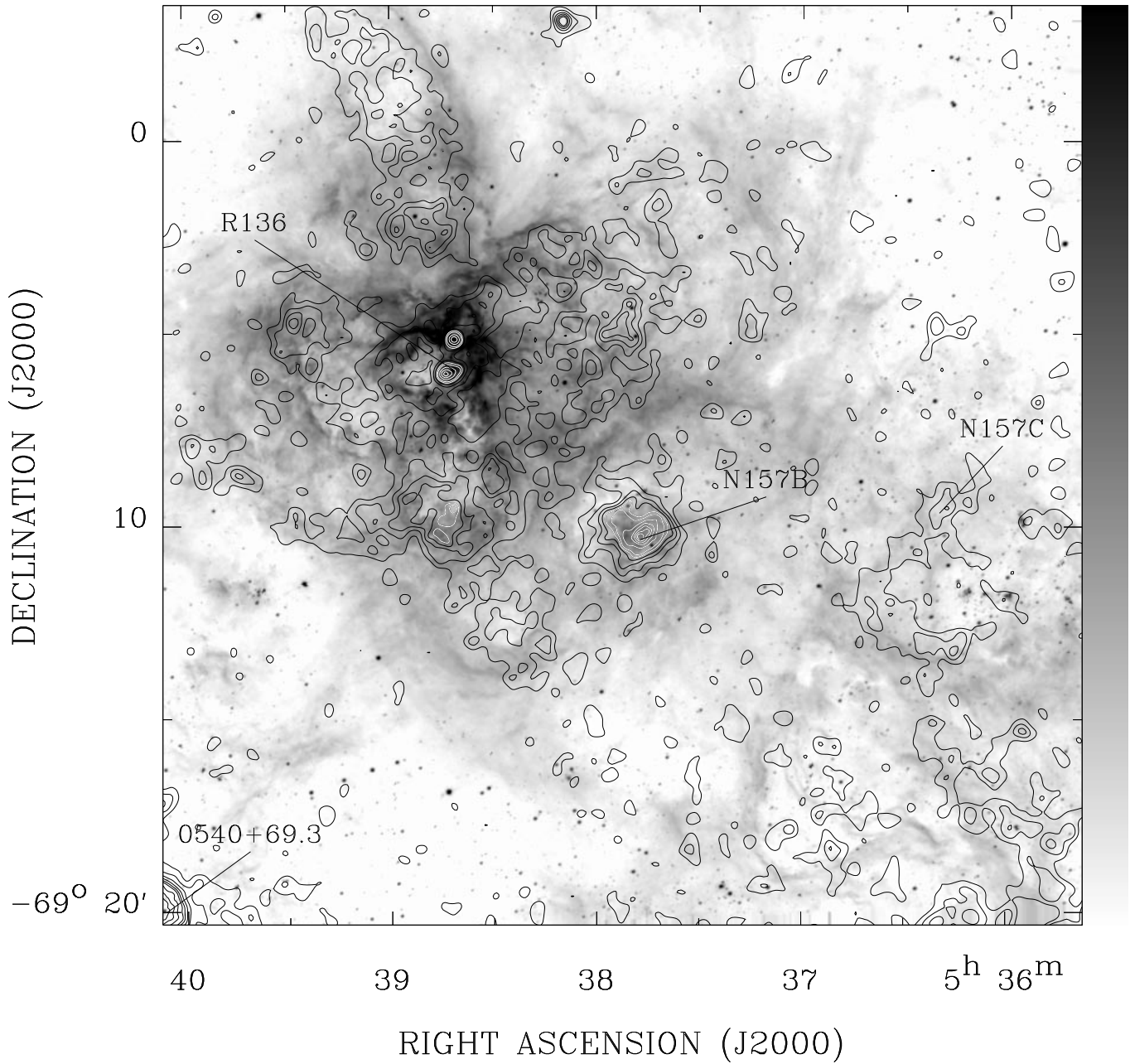
FIG. 2.—N157B and its environment: RHRI X-ray intensity contours overlaid on an Hα image. The X-ray intensity is calculated by co-adding the two background-subtracted RHRI observations and is adaptively smoothed with a Gaussian of adjustable size to achieve a constant local count-to-noise ratio of ~8 over the image. The X-ray contours are at (2.1, 3.8, 5.9, 8.4, 12, 16, 22, 30, 60, 120, 250, 450, and 800) × 10^{-3} counts s^{-1} arcmin^{-2}.

image of the two observations is presented in Figure 2. The processing of the observations was described in an earlier article by Wang (1995), where the same two observations were used to detect two pointlike X-ray sources in the 30 Dor core region and to identify them as Wolf-Rayet + black hole binaries. Briefly, small astrometric errors (~3″) were corrected through comparisons between optical and X-ray positions of identified X-ray sources in the region. Therefore, the absolute astrometric accuracy of the observations is better than ~3″.

The PSPC observation (rp500131), targeted at R136 (Chu 1993), was used to offer a useful combination of moderate spatial resolution (FWHM ~0″.5) and spectral resolving capability (about six independent bands in the 0.1–2 keV range). The spatial resolution of the PSPC, though not as good as that of the RHRI, was still significantly better than the *ASCA* instruments. We extracted a spectrum of N157B from the PSPC observation, using an aperture of 1′.5 for the on-source count rate and an annulus between 2′–3′.5 radii for the background estimation. The aperture is large enough to contain essentially all the counts from the remnant. The total background-subtracted count rate is 0.24 counts s^{-1} in the PSPC 0.1–2 keV band. Similarly, we obtained the RHRI count rate of 0.083 counts s^{-1} in the same aperture.

We found that the PSPC and RHRI observations provided no strong constraints on the timing properties of N157B. The observations were taken in various time segments

spreading over a long period of time—about a half-year in the case of rh600228.

3. ANALYSIS AND RESULTS

3.1. *Timing Properties*

We conducted an extensive search for pulsed emission from N157B. To familiarize ourselves with various methods used, we applied them first to SNR 0540−69.3, which contains a known pulsar. It was easy to detect the pulsar's period of 0.05041843 s, even with one-tenth of the SNR's data. Above 2 keV, the pulsed fraction is 26% ± 2%, almost independent of photon energy. But the fraction falls to 15% ± 2% in the 1–2 keV range and to 9% ± 5% below 1 keV, apparently because of soft diffuse emission from the remnant. No significant periodic signal, however, was detected from N157B, confirming the preliminary conclusion reached by Itoh et al. (1994). In the following, we concentrate on describing our timing analysis of N157B with the GIS data.

We made an fast Fourier transform (FFT) analysis of the combined light curve of the two GIS detectors. This analysis is sensitive to the period range from 3 ms to about 2000 s. The lower boundary is chiefly due to the number of time bins allowed by our computer memory and the upper limit to various observing intervals or gaps on timescales comparable to, or greater than, 2000 s. A single FFT of the light curve is the most sensitive but is limited to the period range longer than 0.05 s. For shorter periods, we first divided the total observing time into up to 16 equal time intervals and then applied FFT separately to the individual light curves. The derived power spectra were averaged to form a combined spectrum, where we found no significant peak. We even tried the incoherent harmonics addition (e.g., Lyne & Graham-Smith 1990) to strengthen harmonics, in case the pulse shape was narrow, but no consistent harmonic pattern was discovered.

We further utilized a period-folding method, but again detected no significant signal. A χ^2 fit with a sinusoidal waveform to a folded pulse profile at an FFT peak period typically yielded a pulsed fraction of ∼6%. By resampling counts according to the "best-fit" model, we estimated a 99% upper limit to the pulsed fraction as ∼9% in the energy band 2–10 keV. The limit for a sharper pulse profile would be tighter. A similar analysis with the PSPC data gave an upper limit as ∼17% in the 0.5–2 keV band.

3.2. *Spatial Properties*

Figures 1 and 2 provide global views of the region including both N157B and the 30 Dor nebula. The RHRI image shows that N157B is well separated from the main body of the 30 Dor nebula. But in the SIS map, scattered X-rays can be considerable near N157B at energies of ≲1.5 keV.

Figure 3 presents close-ups of N157B in the X-ray region, compared with images in Hα and in radio continuum. The northeastern half of the PSPC image (Fig. 3*a*) shows a clear excess of diffuse X-ray radiation, but this diffuse enhancement is harder to see in the raw distribution of RHRI counts (Fig. 3*b*), which include a large number of non–cosmic X-ray events. The low surface brightness diffuse emission is, however, evident in the smoothed RHRI maps (Figs. 3*c* and 3*d*). The distinct part of the enhancement, outlined by the lowest solid contour level (7.4×10^{-3} counts s^{-1} arcmin^{-2}) in Figure 3*c*, is somewhat square shaped and has a dimension of ∼85″ × 85″.

On top of the low surface brightness diffuse X-ray emission is a comet-shaped X-ray feature. The extended morphology of this feature, similar in the two RHRI observations, cannot be due to any instrumental effects. Pointlike objects in the field do not show such elongation (Fig. 2; Wang 1995). This feature has a position angle of ∼38° west to the north. At the southeastern end of the feature is a compact source (R.A. = $5^h37^m47^s.6$; decl. = $-69°10′20″$), which appears extended in rh600228. A maximum likelihood fit to the count distribution of the source suggests count rate of $(25 \pm 5) \times 10^{-3}$ counts s^{-1} and a PSF-subtracted 90% upper limit to the source's full Gaussian size as ∼7″. But an extent of a few arcseconds could be caused by the pointing "jitter" of *ROSAT*. Thus, the source is only marginally resolved, at the best.

A different perspective of the data is presented in Figure 4, where individual cuts of the RHRI intensity distribution are plotted. The compact source of the comet-shaped X-ray feature appears broader than the RHRI PSF (Fig. 4*a*), although part of this broadening may be due to the pointing uncertainty in the observation rh600228. The broad shoulder on the right (northwestern) side of the peak gives an estimate of the length of the X-ray feature as ∼30″ ± 6″. The total width of the feature is ∼20″ ± 4″ (Fig. 4*b*). Table 2 summarizes the properties of the individual X-ray components.

3.3. *Spectral Properties*

Figures 5 and 6 show a remarkable similarity between the SIS spectra of SNR 0540−69.3 and N157B. Both spectra are flat and contain no apparent line features above 1.5 keV, setting these two remnants apart from young shell-like LMC SNRs studied by Hughes et al. (1995). In the SIS spectra of the shell-like SNRs, strong lines *dominate*, and weak continua fall steeply above ∼1 keV.

The spectra of SNR 0540−69.3 and N157B show low energy turnovers at ∼1 keV, indicating that the absorption is mainly due to oxygen and neon. The interstellar abundances of these elements are measured typically within the range between 30% and 40% solar in the LMC (Russell & Dopita 1992; de Boer et al. 1985), and around 40%–60% solar in the solar neighborhood (e.g., Meyer et al. 1994). Because the H I column density of the Milky way in the direction is only $(3.2 \pm 1.3) \times 10^{20}$ cm^{-2} (Bessell 1991), the absorption in the LMC dominates. We assumed an average

TABLE 2

SPATIAL COMPONENTS OF N157B

Component	X-Ray Full Size	Count Rate[a]	Comment
Whole remnant	85″ × 85″	73	≳7.4 × 10⁻³ counts s⁻¹ arcmin⁻²
Comet-shaped feature	30″ × 20″	54	≳2.2 × 10⁻² counts s⁻¹ arcmin⁻²
Compact source	≲7″	25	Probably unresolved

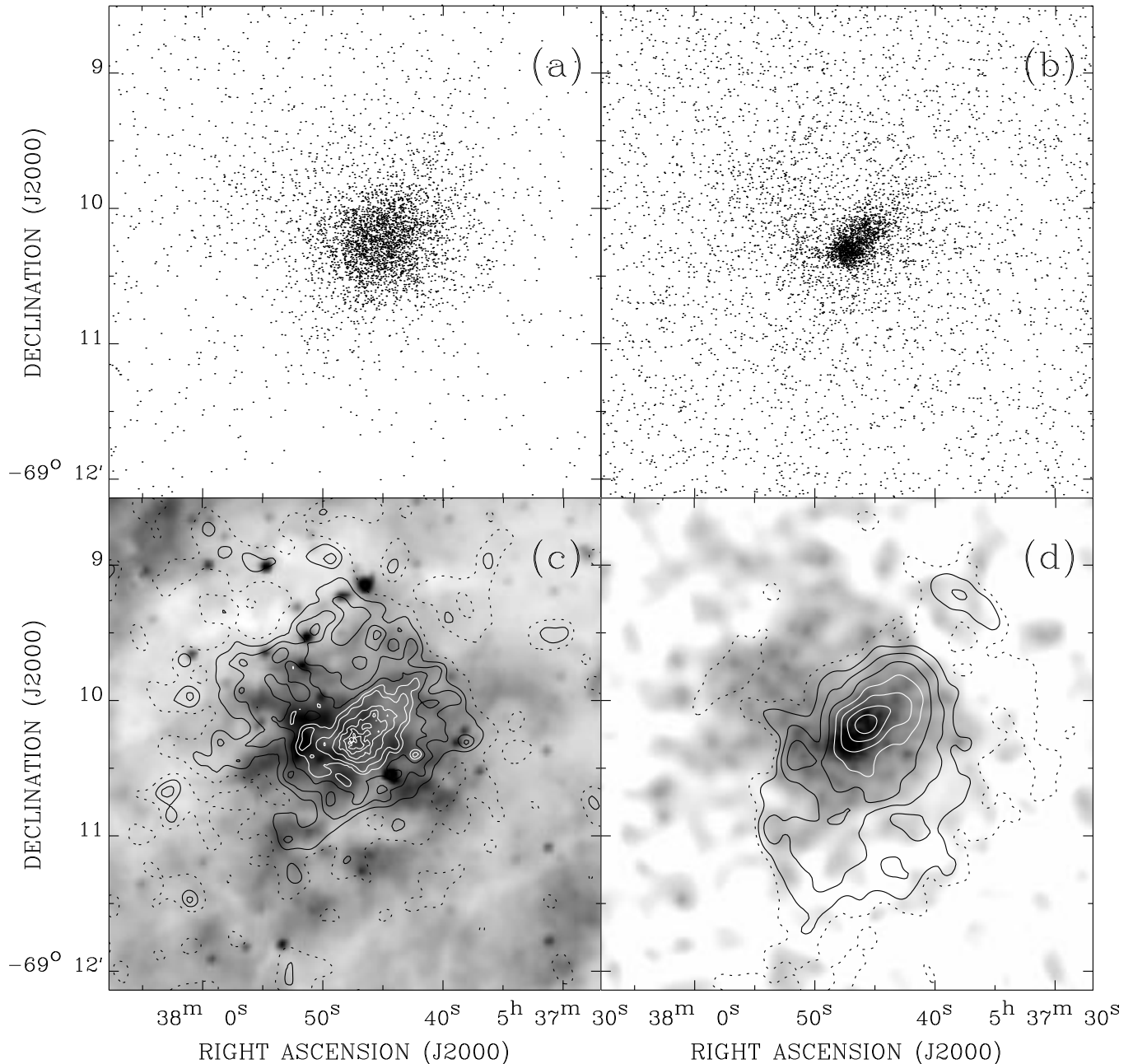[a] In units of 10^{-3} counts s^{-1}.

FIG. 3.—Close-up views of the N157B region: (a) the PSPC count distribution in the 0.5–2 keV band, (b) the RHRI count distribution, (c) the RHRI intensity contours compared with an Hα gray-scale map, and (d) 2.3 GHz continuum intensity contours overlaid on the gray-scaled RHRI map. In (c), the X-ray intensity, background subtracted and exposure corrected, is smoothed with a count-to-noise ratio of ∼4, and the contours are at (3.6, 7.4, 13, 22, 35, 54, 120, 250, 450, and 800) × 10^{-3} counts s^{-1} arcmin^{-2}. In (d), the gray-scaled X-ray intensity is plotted logarithmically in the range between 2.4 × 10^{-3} (about 1 σ above the local background) and 0.5 counts s^{-1} arcmin^{-2}, and the 2.3 GHz radio continuum contours are at 2, 4, 8, 16, 28, 44, 64, and 88 mJy beam^{-1}. The radio data (see also D94) have a FWHM beam size of ∼7″.5, comparable to that of the RHRI image.

metal abundance of 40% solar for X-ray–absorbing gas (Morrison & McCammon 1983) toward both N157B and SNR 0540−69.3. A slightly different choice of the metal abundance would only affect the equivalent hydrogen column density N_H in a spectral fit but would hardly affect the fitting of other spectral parameters. Table 3 summarizes spectral parameters from various fits to the spectral data of the two remnants.

The spectrum of SNR 0540−69.3 is well fitted with a simple power law. The power-law slope is in good agreement with that obtained by Finley et al. (1993), whose analysis is based on a PSPC spectrum and assumes a solar

metal abundance. Switching the abundance in our fit to the solar value and fixing the slope to their best-fit value of 1.0, we obtained almost the same N_H and 0.1–2.4 keV band flux as theirs. This comparison suggests no gross inconsistency between the ROSAT and ASCA data.

A power law, however, does not fit the spectrum of N157B as satisfactorily as that of SNR 0540−69.3. The power-law fit of the N157B spectrum can be rejected at the ≳99% confidence. The residuals of the fit (Fig. 6) exhibit significant systematic fluctuations on energy scales of ∼0.1–0.3 keV, indicating possible emission-line contributions from an optically thin thermal plasma. The feature at ∼0.9
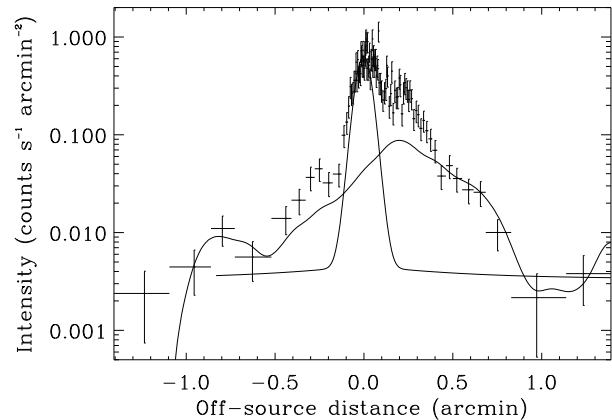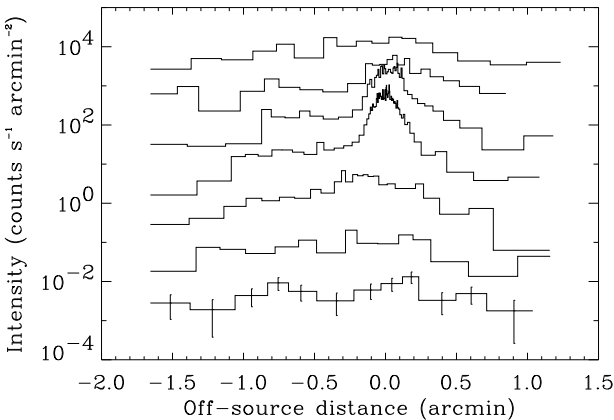
FIG. 4a

FIG. 4b

FIG. 4.—RHRI X-ray intensity distribution in strips across the field of N157B. Each strip is 15″ wide. The histograms are calculated so that each bin has at least 25 counts. Fig. 4a presents a single southeast-northwest cut through the feature (38° west to the north), together with the RHRI PSF (the Gaussian-like profile) and the radio intensity distribution (*solid curve*) in the same cut; the southeast is to the left. The label of the ordinate is for the X-ray data, whereas the radio intensity is in units of Jy beam^{-1}). Fig. 4b includes the northeast-southwest oriented strips, perpendicular to the N157B feature. The northeast is to the left, and the most northwestern strip is at the top. The fourth strip is centered on the position of the compact X-ray source. The bottom histogram is in units as posted; for ease of separation, the intensity in the subsequent histogram is multiplied by 10, and so on.

keV, however, appears a bit too narrow, and its astronomical nature may be questioned, although a stronger line of similar width at ∼1 keV has been reported in the spectrum of the nearby X-ray binary system 4U 1626−67 (Angelini et

al. 1994). Other possible line features are at ∼1.4 keV and 1.8 keV.

To probe the significance of the line features and the thermal plasma component in general, we made a joint spectral analysis of the SIS and PSPC spectra of N157B. First, we fitted the two spectra with a power law, allowing the model normalizations to vary independently. A significant excess around 0.9 keV is apparent in the PSPC spec-
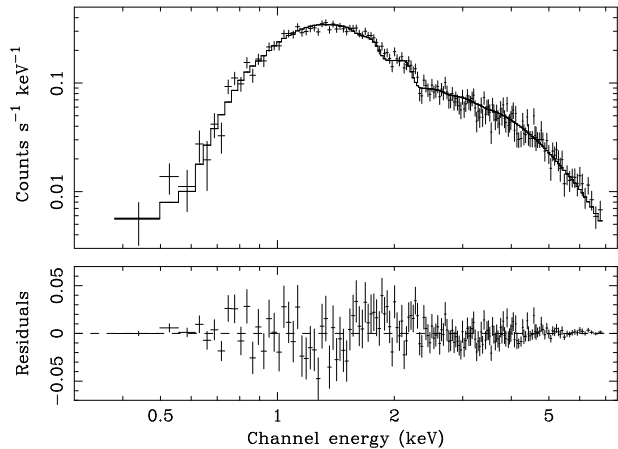

FIG. 5.—*ASCA* SIS spectrum of SNR 0540−69.3. The best-fit power-law model is presented as the histogram. The residuals (spectrum minus model) are shown in the lower panel.
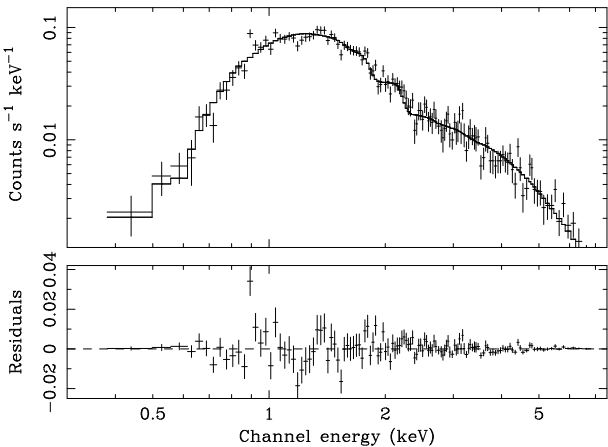

FIG. 6.—*ASCA* SIS spectrum of N157B. The rest is the same as Fig. 5.

TABLE 3

MODEL FIT TO THE *ASCA* AND *ROSAT* SPECTRAL DATA[a]

Data	Model	χ^2/dof	Energy Slope	Column Density[d]	Norm[b]
		SNR 0540−69.3			
SIS..........................	Power law	172/160	1.04 (0.98–1.10)	7.9 (7.4–8.4)	11 (10–12)
		N157B			
SIS + PSPC	Power law + line	171/146	1.4 (1.3–1.5)	6.9 (6.3–7.5)	3.2 (3.0–3.4)[c]
SIS + RHRI (feature)......	Power law	82/78	1.5 (1.4–1.7)	11 (7.3–16)	3.5 (2.8–4.5)
SIS + RHRI (source)	Power law	92/78	1.9 (1.7–2.1)	28 (22–35)	6.1 (4.8–7.4)

[a] The parameter limits are all at the 90% confidence level.
[b] At 1 keV and in units of 10^{-3} photons s^{-1} keV^{-1} cm^{-2}.
[c] From the normalization of the PSPC spectrum.
[d] In units of 10^{21} cm^{-2}.

trum (Fig. 7), which is even greater than that in the SIS spectrum. An inclusion of a simple Gaussian line improves the fit significantly, reducing the χ^2/dof from 197/150 to 171/146; the excess is gone in the residuals for both the SIS and PSPC spectra (Fig. 8; Table 3). The line in the PSPC spectrum has a flux of 3.5 (2.4–5.5) $\times$ 10^{-4} photons s^{-1} cm^{-2} at 0.9 (0.89–0.92) keV. The flux in the SIS spectrum is, however, only 45% (21%–68%) of that in the PSPC spectrum, whereas the power-law normalizations in the SIS and PSPC spectra are very close (within $\sim 5\%$). This line flux discrepancy can be explained if the thermal component originates in the low surface brightness diffuse emission region (Table 2). Part of the diffuse emission is not accounted for in our extraction of the SIS spectra, which assumes the remnant to be pointlike.

We further tried the standard collisionally equilibrium plasma model (i.e., Raymond & Smith 1994, hereafter R&S). For simplicity, we discuss here only the results from the fits to the SIS spectrum. A single-temperature model fit is not satisfactory; the best-fit model is much steeper than the SIS spectrum at energies $\gtrsim 4$ keV. Such a thermal model is, however, perfectly acceptable for the *Einstein* solid state spectrometer (SSS) data, partly because of the instrument's narrower energy coverage $\lesssim 4$ keV. The absorption inferred

from the SSS spectrum is also significantly smaller than the value obtained from the *ASCA* data. We suspect that this is caused by a considerable soft X-ray contribution from the main body of 30 Dor within the SSS aperture of $\sim 6'$ diameter. Therefore, the results from the SSS spectrum should be used with caution. A two-component model consisting of a power law and an R&S plasma improves our power-law fit to the SIS spectrum only slightly (χ^2/dof = 164/125); the thermal component, even with the abundance allowed to vary, does not adequately account for the apparent line features. Without accurate information on the remnant's environment, structure, and evolution, we are unable to use the limited statistics and line signatures of the data to explore the vast parameter space of more sophisticated models.

The power-law contribution may be determined, however, if it is solely due to the comet-shaped feature, presumably a synchrotron nebula (§ 4.3). We used the RHRI count rate of 0.054 counts s^{-1} (Table 2; with an estimated uncertainty of $\sim 20\%$) to isolate the contribution of the feature below 2 keV. At higher energies, where the thermal contribution may be neglected, we used the SIS spectrum. The spectral parameters from a power fit to this SIS/RHRI combined spectral data are included in Table 3. Because of the exclusion of the diffuse component, the $N_{\rm H}$ value is greater than those from the previous fits. The luminosity of the power-law component is $L_x = 1.0 \times 10^{36}$ ergs s^{-1} in the 2–7 keV band, or $L_x = 5.6 \times 10^{36}$ ergs s^{-1} in the 0.2–4 keV band. The uncertainties of these luminosity estimates are $\sim 30\%$.

Figure 9 presents the power-law model, together with the SIS spectrum including data points below 2 keV. The residuals, evidently showing line features, do appear to be thermal in origin. A fit with a single-temperature R&S model suggests a characteristic plasma temperature of ~ 0.7 keV. However, the fit (χ^2/dof = 187/128) is not satisfactory; there is a significant excess above the model below 0.7 keV. A similar fit (χ^2/dof = 21/26) to the residuals in the PSPC spectrum is good, and the best-fit temperature is 0.41 (0.31–0.53) keV. Thus, the thermal model describes the residuals well only at the PSPC's resolution. The predicted RHRI count rate ~ 0.031 counts s^{-1} is consistent with the rate of
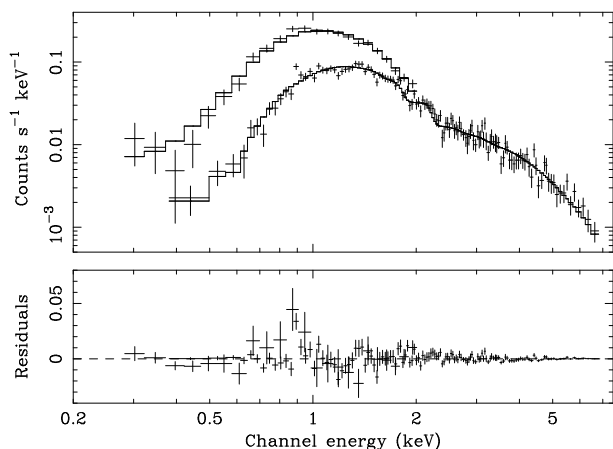

FIG. 7.—Joint power-law fit to the *ASCA* and PSPC spectra of N157B. The rest is the same as Fig. 5.
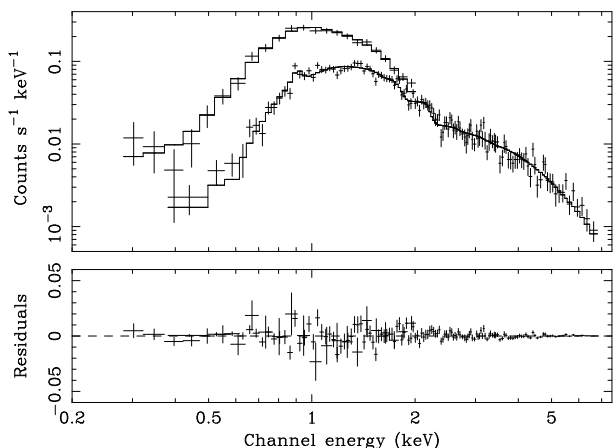

FIG. 8.—Joint fit to the *ASCA* and PSPC spectra of N157B with a two-component model consisting of a power law and a Gaussian line. The rest is the same as Fig. 5.
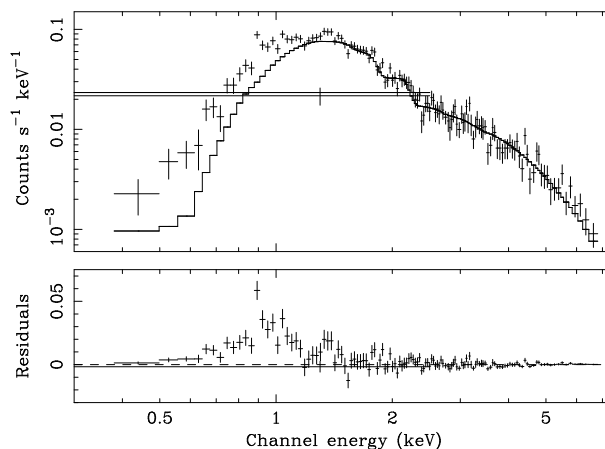

FIG. 9.—*ASCA* spectrum of N157B and the best joint fit of a power law to both the spectrum above 2 keV and the RHRI flux of the comet-shaped X-ray feature (§ 3.3). The RHRI data point has its energy coverage between the 0.3–2.4 keV range. The residuals of the fit are shown in the lower panel.

the diffuse component within an estimated systematic error of up to $\sim 40\%$.

The above isolation of the power-law component is physically plausible, but it is not unique. Alternatively, the power-law component might arise only in the compact X-ray source. A power-law fit to this combination (Table 3), however, is not as satisfactory. In particular, the absorption appears much too large (by a factor of ~ 3) to be consistent with the measurement of the optical extinction toward N157B (§ 4.4).

4. DISCUSSION

4.1. *Qualitative Considerations*

The striking similarity between the spectra of N157B and SNR $0540-69.3$, together with the centrally peaked morphology of N157B in both radio and X-rays, leaves little doubt about N157B as a Crab-like SNR. In contrast to the highly polarized emission observed in the Crab and SNR $0540-69.3$, however, no radio polarization has been detected in N157B (D94).

The comet-shaped X-ray feature is evidently the most interesting emission component of N157B. Markwardt & Ögelman (1995) have observed a morphologically similar feature near the Vela pulsar. They interpret this feature as the thermal emission from a cocoon around a jet from the pulsar. The pulsar's proper motion is found to be nearly perpendicular to the direction of the jet. Therefore, it is possible that the jet is sweeping up the ambient material, which may explain the apparent higher density in the cocoon than in the ambient medium. However, the X-ray luminosity of the N157B feature is more than 3 orders of magnitude greater than that ($\sim 10^{33}$ ergs s^{-1}) of the Vela jet. Furthermore, the *ASCA* spectrum shows that the emission, most of which arises in the comet-shaped feature, is predominantly nonthermal in origin (§ 3.3).

4.2. *Low Surface Brightness Diffuse X-Ray Emission*

The diffuse emission component of N157B most likely arises in a diffuse plasma, which is responsible for the possible weak line features in the *ASCA* spectrum. We adopt a conversion of an RHRI count rate to an emission integral (EI; defined as $\int n_e^2 \, dV$) as 2.7×10^{60} cm^{-3} (counts s^{-1})$^{-1}$. This conversion applies to the model of $N_H \sim 10^{22}$ cm^{-2} and $T \sim 0.7$ keV and is good within a factor of 2 as long as the temperature $\gtrsim 0.4$ keV. From Table 2, we infer a count rate of the diffuse component as 0.019 counts s^{-1}, corresponding to an EI of 5.0×10^{58} cm^{-3} and an X-ray luminosity as 1×10^{36} ergs s^{-1} in the 0.1–2.4 keV band, or 0.7×10^{36} ergs s^{-1} in the 0.5–2 keV band. Further assuming that the diffuse component arises in an approximately spherical space of diameter $D = 20$ pc, and using ζ as the effective spatial filling factor, we estimate the gas density n_h as $\sim 0.6 \zeta^{-0.5}$ cm^{-3}. The corresponding total gas mass is then $\sim 56 \zeta^{0.5} M_\odot$. If $\zeta \gtrsim 0.1$, the remnant expansion should then be in the Sedov phase (e.g., Cox 1972). The total thermal energy in the X-ray–emitting plasma is $\sim 3 \times 10^{50} \zeta^{0.5}$ ergs, a considerable fraction of the expected mechanical energy of a supernova (SN). Because this fraction is expected to be $\sim 72\%$ in the Sedov phase, the inferred SN energy is in a nominal range of a few times 10^{50} ergs. Finally, the Sedov age of the remnant is $t_{SNR} = 5 \times 10^3 D_{20\,pc} T_{0.7\,keV}^{-1/2}$ yr, where $D_{20\,pc}$ is the remnant diameter in units of 20 pc and $T_{0.7\,keV}$ the diffuse plasma temperature in units of 0.7 keV.

Both the above X-ray size and boundary agree with those inferred from kinematic studies of Hα-emitting gas in N157B (e.g., CKSL92). These studies have revealed shocked materials with velocity offsets up to $\sim 10^2$ km s^{-1}. However, since the velocity of Hα-emitting gas does not necessarily represent the expansion of the outer shock of the N157B remnant, the inferred characteristic age can, at most, be considered as an upper limit to the true age of the remnant.

4.3. *Comet-shaped X-Ray Feature*

The predominant nonthermal nature of N157B leads us to explain the comet-shaped X-ray feature as a synchrotron nebula, powered by the putative pulsar embedded in N157B. This explanation, constrained by the observations, provides specific predictions about the energetics and dynamics, as well as the spatial and spectral properties of the remnant.

From the luminosity of the X-ray feature, $L_x = 5.6 \times 10^{36}$ ergs s^{-1} in the 0.2–4 keV band (§ 3.3), we may estimate the spin-down power $\dot{E}$ of the pulsar. A linear relation $\log L_x \approx 1.39 \log \dot{E} - 16.6$, obtained by Seward & Wang (1988), fits reasonably well to the three confirmed Crab-like SNRs. Applying this relation to N157B, we obtain $\dot{E} \approx 2 \times 10^{38}$ ergs s^{-1}. Following Seward & Wang (1988) again, we further estimate the period and magnetic field strength of the pulsar as $\sim (0.08 \text{ s})(t_3 \dot{E}_{38})^{-1/2}$ and $\sim (1 \times 10^{13} \text{ G}) t_3^{-1} \dot{E}_{38}^{-1/2}$, where t_3 is the remnant's age in units of 10^3 yr.

The steep X-ray spectrum provides clues about the energy-losing mechanism of relativistic particles in the synchrotron nebula. The X-ray–emitting lifetime t_x of an electron in the nebula can be expressed as

$$t_x \sim (40 \text{ yr}) \epsilon^{-1/2} (H_{-4})^{-3/2} , \qquad (1)$$

where ϵ is the characteristic synchrotron photon energy in units of keV and H_{-4} is the magnetic field in units of 10^{-4} G. This timescale is much shorter than the expected age of the remnant. Therefore, a steady pulsar spin-down luminosity is a good approximation to model the current X-ray emission from the nebula. We assume that the distribution of pulsar injected particles is approximately a power law with an index of γ and that the velocity distribution is isotropic. The X-ray emission spectrum is then a power law with $\alpha = \gamma/2$ if synchrotron radiation loss dominates, or $\alpha = (\gamma - 1)/2$ if the energy loss is predominately due to adiabatic expansion of pulsar wind materials (e.g., Tucker 1977). In general, one expects a convex-shaped spectrum: the adiabatic loss dominates at low energies, whereas the synchrotron becomes important at high energies. Such a slope change from high to low energies is a general characteristic of Crab-like SNRs (e.g., Du Plessis et al. 1995). The steep spectrum observed in N157B thus suggests that the synchrotron loss dominates in N157B even in the relatively low energy range of 0.5–7 keV. From the slope of ~ 1.5 (§ 3.3), we obtain $\gamma \sim 3$.

The spatial properties of the comet-shaped X-ray feature have implications for the dynamics of relativistic electrons. Because of the short lifetime of the electrons, the size of a synchrotron nebula should typically be much smaller than that of the corresponding radio one if electrons diffuse through the nebula medium at the Alfvén velocity. The observed size and comet-like shape of the X-ray feature suggest that X-ray–emitting particles are undergoing an

outflow, which can travel much faster than diffusing electrons. The compact source, where energy is likely being deposited by the pulsar, is separated from the radio peak (§ 4.4), where most of the pulsar spin-down energy has supposedly been dumped. If the *birth*place of the pulsar is close to the position of the radio peak and has an age of $\sim 5 \times 10^3$ yr (§ 4.2), the separation of $\sim 12''$ between the pulsar and the radio peak then implies that the pulsar has a transverse velocity of $\sim 6 \times 10^2$ km s^{-1}, compared to an average pulsar velocity of $\sim 4 \times 10^2$ km s^{-1} (Lyne & Lorimer 1994). We use $v_{p,3}$ (in units of 10^3 km s^{-1}) to characterize the total velocity of the pulsar motion.

Such a relatively fast moving young pulsar can produce a strongly elongated pulsar wind bubble (Fig. 10). This bubble consists of several distinct regions. First, one may expect a bow shock running ahead of the pulsar, while the corresponding reverse shock terminates the free pulsar wind. The size of the region enclosed by this bow shock can be small, but the pressure can be large, depending on the ram pressure. Enhanced synchrotron radiation can then make the region especially bright in the X-ray region. Second, accelerated by the pressure gradient between the bow shock and the ambient medium, the shocked wind materials, which are relativistically hot, naturally forms a supersonic jet inside a tunnel in the opposite direction of the pulsar's motion (Wang, Li, & Begelman 1993). Third, the jet likely shoots through the bubble and then induces another bow shock (or a series of oblique shocks) on the other side. Fourth, the terminated wind materials are forced back to the bubble, where most of the pulsar spin-down luminosity is dumped. Let us now examine this picture in a more quantitative way.

The size of the bow shock region around the pulsar should be consistent with the observed upper limit. The characteristic reverse shock radius r_s is defined by the ram-pressure balance between the pulsar wind and the pulsar motion,

$$r_s = (4 \times 10^{-2} \text{ pc})[\dot{E}_{38}/(n_a v_{p,3}^2)]^{1/2} , \qquad (2)$$

where $\dot{E}_{38}$ is the spin-down luminosity in units of 10^{38} ergs s^{-1} and n_a is the ambient medium density, which may be of the same order of magnitude as n_h estimated in the diffuse X-ray emission (§ 4.2). The size and shape of the outer bow shock depend critically on the dynamical effect of magnetic fields, and no theoretical model has yet been developed to describe this phenomenon. We thus characterize the total
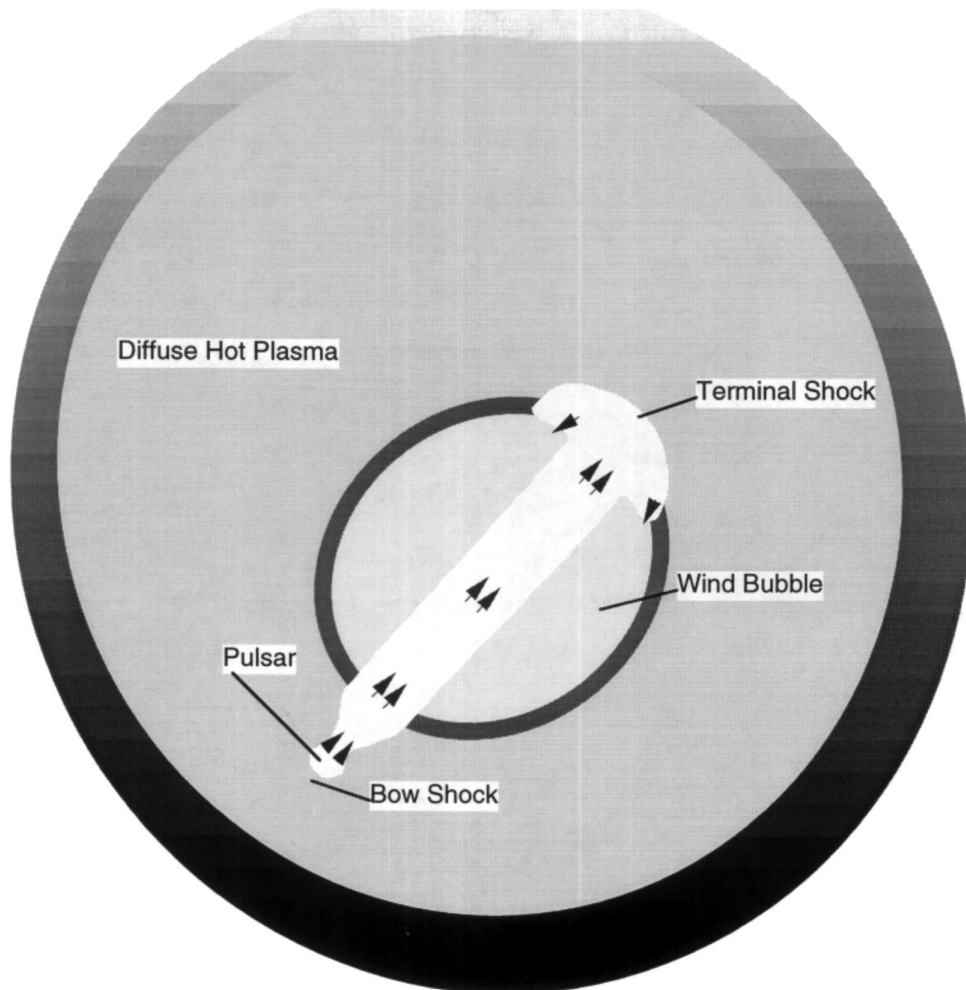

Fig. 10.—Illustration of the current pulsar position and the flow of pulsar wind materials interacting with the N157B remnant. The arrows represent the flow of the materials. The remnant's blast wave is represented by the outer shell. The configuration of the components is somewhat similar to the fan-shaped radio feature connecting the pulsar PSR 1757−24 and the SNR G5.4−1.2 (Frail & Kulkarni 1991).

volume of the region enclosed by the bow shock as $V_x = (4/3)\pi(\xi r_s)^3$, where the parameter ξ is to be constrained. Assuming that the energy is partitioned equally between particles and magnetic fields, that the field is randomly distributed, and that the pressure is balanced in the region, we have

$$H \approx (0.8 \text{ mG})(n_a v_{p,3}^2)^{1/2} , \tag{3}$$

$$W_e = \frac{H^2}{8\pi} V_x , \tag{4}$$

where W_e is the total energy in particles. Since only about half of the observed X-rays from the feature originates in the compact X-ray source (Table 2), the time spent by the shocked pulsar wind materials in the bow shock region is probably comparable to the lifetime of an electron that emits 1 keV photons. For a steady jet, we expect

$$W_e \sim t_x \dot{E} = (5 \times 10^{44} \text{ ergs})\dot{E}_{38}(n_a v_{p,3}^2)^{-3/4} . \tag{5}$$

From (2)–(5), we obtain

$$\xi \sim 3\dot{E}_{38}^{-1/6}(n_a v_{p,3}^2)^{-1/12} . \tag{6}$$

The bow shock has a size $\sim 2\xi r_s \sim 1''\dot{E}_{38}^{1/3}(n_a v_{p,3}^2)^{-7/12}$, consistent with the upper limit to the full size of the compact X-ray source ($\lesssim 7''$; Table 2).

After being forced out from the bow shock, the wind materials can continue to radiate in the X-ray region (Fig. 10). The radiation from the relativistic jet itself (Wang et al. 1993), however, may not be significant. Most of the X-rays from the comet-shaped feature outside the compact X-ray source are probably released after the jet is terminated and are from shocked wind materials inside the bubble, explaining why the width of the X-ray feature (Table 2) is comparable to that of the compact radio emission region (§ 4.4). Just like particles in the bow shock region, the shock materials in the wind bubble are still relativistically hot, and the emission is primarily synchrotron.

4.4. *Radio Emission*

We speculate that the lack of polarization in the observed radio emission of N157B is due to the presence of a giant H ɪɪ region produced by the coexisting OB association LH99 (Schild & Testor 1992). CKSL92 find that about 20% of the radio emission arises in the H ɪɪ region, to be consistent with both the Hα-to-radio continuum ratio and the average extinction ($A_v = 1.0$ mag), inferred from Balmer decrement measurements over a 4.9 region surrounding N157B (Caplan & Deharveng 1985). The rest of the radio emission is presumably nonthermal; part of the emission should be associated with the synchrotron nebula of the N157B remnant. The radio emission above the level of 28 mJy beam^{-1} in Figure 3d has an extent similar to the X-ray feature, but the centroid of the emission feature is about $12'' \pm 3''$ away from the compact X-ray source. Based on the relations $A_v/E(B-V) = 3.1$ and $N_{\rm H}/E(B-V) = 2.4 \times 10^{22}$ cm^{-2}, which are appropriate for the interstellar gas in the 30 Dor region (Fitzpatrick 1986), we infer $N_{\rm H} = 7.7 \times 10^{21}$ cm^{-2}. In comparison, our X-ray-measured $N_{\rm H}$ is $\sim 1 \times 10^{22}$ cm^{-2} (§ 3.3). Thus the N157B remnant is likely located in or behind the H ɪɪ region.

The ionized gas and the expected magnetic field of the H ɪɪ region can cause Faraday rotation in the radiation from the synchrotron nebula. Assuming that the 20% of the observed radio emission arises in a spherical region of ~ 20 pc diameter, similar to the projected dimension, we estimate a mean free electron density $n_e \sim 50$ cm^{-3}. The Faraday rotation angle varies with $n_e H_\parallel$, where $H_\parallel$ is the line-of-sight intensity of the field. Following Burn (1966), we express the dispersion of the rotation within a radio survey beam as

$$\delta\phi \sim [K n_e H_\parallel d_e \lambda^2] d_s/d_e , \tag{7}$$

where the coefficient $K = 2.6 \times 10^{-17}$, d_e is the characteristic size of turbulent eddies, $d_s = 1.8$ pc and $\lambda = 13$ cm are the beam size and the wavelength of the 2.3 GHz survey. In the bracket of the above equation is the Faraday rotation angle through a single eddy. Assuming a typical interstellar field of $H_\parallel \sim 5\mu$G, we obtain $\delta\phi \sim 6$. This dispersion produces a radiation depolarization

$$p \sim p_i \exp\left[-2(\delta\phi)^2 d_{\rm H\,II}/d_e\right] , \tag{8}$$

where d_e should be comparable to, or smaller than, the dimension $d_{\rm H\,II}$ of the region. Therefore, only if a fraction of the observed H ɪɪ region is in front of the nebula can the Faraday dispersion explain the lack of the polarized emission in the 2.3 GHz survey. Clearly, a radio survey at a higher frequency will have a better chance to detect the polarized emission from the synchrotron nebula.

5. SUMMARY

Based on the *ROSAT* and *ASCA* observations, we have examined the X-ray timing, spatial, and spectral properties of N157B. An algorithm has been devised for extracting *ASCA* spectra for a pointlike X-ray source. For comparison, we have also presented an *ASCA* spectrum of SNR 0540−69.3, the only LMC SNR that contains a detected pulsar. We have arrived the following main results and conclusions.

1. The flat and featureless spectrum of N157B in the 2–7 keV range resembles that of SNR 0540−69.3, and is distinctly different from those of young shell-like SNRs in the LMC. The power-law energy slope (~ 1.5) of the spectrum is, however, steeper than those (~ 1.0) of SNR 0540−69.3, MSH 15−52, and the Crab nebula.

2. The *ASCA* spectrum of N157B shows possible line features at energies $\lesssim 2$ keV. A joint analysis of the *ASCA* and *ROSAT* data suggests that these features are likely associated with a thermal emission component of the remnant.

3. No pulsed signal is identified; the pulsed fraction is $\lesssim 17\%$ of the remnant's total luminosity in the 0.5–2 keV band, or $\lesssim 9\%$ in the 2–10 keV band. So the putative pulsar in N157B is still elusive.

4. More than two-thirds of the observed X-ray radiation from N157B comes from a comet-shaped X-ray feature, which has a size of $\sim 7 \times 5$ pc and a luminosity of $\sim 1 \times 10^{36}$ ergs s^{-1} in the 2–7 keV range.

5. We interpret the X-ray feature as the synchrotron radiation from pulsar wind materials. The pulsar is likely moving at a speed of $\sim 10^3$ km s^{-1}. A ram-pressure confined bow shock around the pulsar may account for an embedded compact X-ray source, which is probably unresolved. The ram pressure further focuses fresh wind

materials into a relativistic jet. The jet is eventually terminated on the other side of the pulsar wind bubble, where most of the spin-down energy has been dumped.

6. Around the X-ray feature, we further detect a low surface brightness diffuse X-ray emission region. This region most likely accounts for the apparent thermal component in the *ROSAT* and *ASCA* spectra below ~ 2 keV. The remnant has a diameter of ~ 20 pc and a 0.5–2 keV luminosity of $\sim 7 \times 10^{35}$ ergs s^{-1}, a total thermal energy of $\sim 3 \times 10^{50}$ ergs, and an age of $\sim 5 \times 10^3$ yr.

7. The lack of polarized radio emission from N157B may be explained by the depolarization of a foreground H II region.

APPENDIX A

ASCA BACKGROUND SPECTRAL ESTIMATION FOR AN ISOLATED POINT SOURCE

A1. INTRODUCTION

Estimating a local background spectrum and subtracting it from an on-source X-ray spectrum normally represents a crucial step in analyzing the spectral properties of a source. Because of the broad *ASCA* PSF (see § 2.1), it is not usually practical to obtain an independent measurement of the background free of source contamination without going far from the source, where data might not exist, or the background might differ significantly. For example, an annular background region of radius 3′–5′ would require that the source count rate be less than 0.03 counts s^{-1} for it not to contribute more than 10% to the total counts in the background region. This count rate is barely detectable in a typical 20 ks observation. For an observation of a moderately bright point source, the counts in the background are an admixture of source and background counts. On the other extreme, a source of a few count per second would dominate the background region, contributing greater than 90%, and the background can be ignored to the first order. We are interested here in the intermediate case.

The measured background includes X-rays of cosmic origin, X-rays, and particles of solar origin, cosmic-ray–induced X-rays, and internal instrumental counts. Perhaps most insidious for *ASCA* is the stray light X-rays (mirror rays that undergoes single, instead of double, reflections, etc.), which are not imaged in the usual way, and which depends strongly on the celestial distribution of X-ray emission in and out ($\lesssim 1°$) of the telescope's field of view. The background depends on the satellite geographical location and height above the Earth, solar activity, and the incident cosmic X-rays, as well as telescope pointing angle relative to the Earth, Sun, and Earth's magnetic field vector. Taken together, these produce a background for a given observation whose spectrum and intensity depends on date, orbit, sky, and detector coordinates. The broad PSF wings also mean that other sources in the field may substantially color the target spectra, producing an additional effective background.

The current recommended practice for estimating the background is to extract counts from the *ASCA* Deep Field pointings, screened in a manner identical to the data, and selected from the source detector region. For the simple case of an isolated point source, using the Deep Fields should give a reasonable zeroth-order estimation of the background. However, for a given observation and target, this practice is limited by the uniqueness of background as discussed above. As an added complication, although these fields might represent the background statistically in an average field, they are known to contain explicit point sources, which may compromise extracted spectra near their detector locations. Furthermore, the response of the detector to the background changes over the course of the mission due to known secular degradation of the instruments with time. Most important, the background intensity and spectrum can vary from one field to another, especially in regions of nearby galaxies such as the LMC.

Here, we present a simple method for a first-order estimate of both the source spectrum and the background spectrum from the data itself, for the case of an isolated point *ASCA* source embedded in a statistically uniform local background. The advantage of self-calibrating is evident given the strong temporal, instrumental, orbital, and celestial dependence of the background. Our method is to consider the spectral ratio of observed and expected counts in concentric annuli centered on the source, each of which is an admixture of the true source and background spectrum. We look for deviations of the radial average profile from that expected for a point source and simultaneously solve for the two spatially distinct spectral components. Thus we can estimate the background over the source region itself. This is in effect a form of spectrospatial deconvolution of the background and source spectra.

A2. METHOD

Consider the observed counts in two concentric regions centered on the source and in the measured spectral bin ("PHA" bin) E', $O_1(E')$ and $O_2(E')$, both of which are a composition of the source and background spectra, $S(E')$ and $B(E')$, respectively,

$$O_1(E') = \rho_1(E)S(E') + \alpha_1 B(E') , \tag{A1}$$

$$O_2(E') = \rho_2(E)S(E') + \alpha_2 B(E')v(E) , \tag{A2}$$

where α_1, α_2 are the geometric areas of the respective regions; $v(E)$ is the mean vignetting of the background region relative to the source; $\rho_1(E)$ and $\rho_2(E)$ are the encircled energy function[2] v(EEFs) within those areas. Here the energy, E, refers to the

energy dependence of $\rho(E)$ and $v(E)$, which also depend on specific locations of α_1 and α_2 in detector coordinates. These dependencies have been modeled with laboratory and on-orbit calibrations, and therefore the ratios $\gamma = \alpha_1/v(E)\alpha_2$ and $\delta = \rho_1/\rho_2$ are determined. Notice that these ratios are not strongly energy dependent below ~ 6 keV and, for most cases, to the limit of our approximation, a single number for each is reasonable.

We can then solve for the source and background spectra and find

$$\rho_1(E)S(E') = \delta(O_1(E') - \gamma O_2(E'))/(\delta - \gamma) , \tag{A3}$$

$$\alpha_1 B(E') = \gamma(O_1(E') - \delta O_2(E'))/(\gamma - \delta) , \tag{A4}$$

where $\rho_1 S(E')$ is the total counts enclosed in the source area α_1 in spectral bin E' and $\alpha_1 B(E')$ is the background spectra over the same area at that energy. The coefficients of $S(E')$ and $B(E')$ insure correct normalization and units. The resulting errors for the source and background are simply found from the quadratic sum of the errors associated with individual terms.

In practice, we carry out this calculation on each PHA (PI) bin in our spectral file. The energy dependencies (E) and (E') are related by the spectral redistribution file, $\mathrm{RMF}(E; E')$, and do not enjoy a one-to-one correspondence. However, our method is insensitive to this redistribution, as it is a third-order effect because it arises in the errors in the ratios γ and δ, which come from the fraction of redistributed counts at the lower energies. The typical negative sloped spectra and the weak energy dependence of these ratios insure that this effect is negligible for our purpose.

For simplicity, we assume the ratios γ and δ are energy independent. We can then easily compute the source and background spectral components using the FTOOL MATHPHA to perform the calculation on each element of the spectral ("PHA") file. We are then left with a spectral file that can be imported directly into a spectral analysis package such as XSPEC. These spectra will be correctly normalized, and the instrument and mirror response files ("RMF" + "ARF")[3] created for $O_1(E')$ are still appropriate. It is most practical to use the observed source spectra $O_1(E')$ along with the derived background spectra $\alpha_1 B_1(E')$ in analyzing the source spectra.

The energy dependence of $\rho(E)$ and $v(E)$ can be explicitly accounted for by using the Awaki's "XRTEA" effective area subroutine, which returns $\rho(E)$ and $v(E)$ as a function of source position in a detector and off-source angle. This code is available in the FTOOLS software package. An attractive alternative for measuring the EEF is to use an observation of a bright pointlike source. If this fiducial source is acquired at the same detector position (i.e., 1-CCD mode default) as the source under study, and the data screened and exposure corrected in the same way, then the background for the fiducial source relative to the study source may be reasonably ignored. Modeling the EEF with a real observation allows for the jitter in the attitude, which is similar from observation to observation (order $\lesssim 10''$). For the SIS, the fiducial source should not be too bright as to be noticeably affected by pileup. The bright cataclysmic variables make excellent targets and have been successfully used for this purpose.

In conclusion, the above method allows an estimate of the background spectrum under a circular aperture, centered on a pointlike source. Given enough counts, this method can naturally extend to a least squares solution for a general spectro-spatial deconvolution for a point source. We may extract counts from a set of N concentric annuli and solve the set of linear equations of the form

$$O_n(E') = \rho_n(E)S(E') + \alpha_n B(E')v_n(E) . \tag{A5}$$

---

[2] The unfortunate use of the term "energy" here is not to be confused with the spectral energy, as it in fact refers to the power contained in the mirror PSF at various radii; it is defined as the relative counts ("energy") enclosed in the PSF between the radii a and b, $\mathrm{EEF}(E; a, b) = \int_a^b \mathrm{PSF}(E)/\int_0^\infty \mathrm{PSF}(E)$.

[3] A description of the "PHA," "ARF," and "RMF" files, the XSPEC spectral analysis program, and the FTOOLS software package is available in the *ASCA* data analysis guide (Day et al. 1995) and references therein.

REFERENCES

Angelini, L., et al. 1994, BAAS, 185, 6206
Bessell, M. S. 1991, A&A, 242, L17
Burn, B. J. 1966, MNRAS, 133, 67
Caplan, J., & Deharveng, L. 1985, A&AS, 62, 63
Chu, Y.-H. 1993, in AIP Conf. Proc. 313, The Soft X-Ray Cosmos, ed. E. M. Schlegel & R. Petre (AIP: New York), 154
Chu, Y.-H., Kennicutt, R. C., Jr., Schommer, R. A., & Laff, J. 1992, AJ, 103, 1545 (CKSL92)
Clark, D. H., et al. 1982, ApJ, 255, 440
Cox, D. P. 1972, ApJ, 178, 159
Day, C. S. R., et al. 1995, The ABC Guide to *ASCA* Data Reduction, *ASCA* Guest Observer Facility (Greenbelt: NASA/GSFC) (http://heasarc.gsfc.nasa.gov/docs/software/ftools/ftools_menu.html)
de Boer, K. S., Fitzpatrick, E. L., & Savage, B. D. 1985, MNRAS, 217, 115
Dickel, J. R., et al. 1994, AJ, 107, 1067 (D94)
Du Plessis, I., et al. 1995, ApJ, 453, 746
Finley, J. P., Ögelman, H., Hasinger, G., & Trümper, J. 1993, ApJ, 410, 323
Fitzpatrick, E. L. 1986, AJ, 92, 1068
Frail, D. A., & Kulkarni, S. R. 1991, Nature, 352, 785
Gotthelf, E. V. 1993, CLEANSIS, FTOOLS Software Package, HEASARC (Greenbelt: NASA/GSFC) (ftp legacy.gsfc.nasa.gov)
Gould, A. 1995, ApJ, 452, 189
Hirayama, M., et al. 1996, *ASCA* News, No. 4, 18

Hughes, J. P., et al. 1995, ApJ, 444, L81
Itoh, M., et al. 1994, New Horizon of X-Ray Astronomy, ed. F. Makino & T. Ohashi (Tokyo: Universal Academy Press), 507
Jahota, L., Gotthelf, E. V., & Zoonematkermani, S. 1993, SPIE, 4541, 453.
Lyne, A. G., & Graham-Smith, F. 1990, Pulsar Astronomy (Cambridge: Cambridge Univ. Press)
Lyne, A. G., & Lorimer, D. R. 1994, Nature, 369, 127
Markwardt, C. B., & Ögelman, H. 1995, Nature, 375, 40
Mathewson, D. S., et al. 1983, ApJS, 51, 345
Meyer, D. M., et al. 1994, ApJL, 437, 59
Mills, B. Y., Turtle, A. J., & Watkinson, A. 1978, MNRAS, 185, 263
Morrison, R., & McCammon, D. 1983, ApJ, 270, 119
Raymond J., & Smith, B. W. 1994, XSPEC User's Guide for Version 8 (Greenbelt: NASA/GSFC)
Russell, S. C., & Dopita, M. A. 1992, ApJ, 384, 508
Schild, H., & Testor, G. 1992, A&AS, 92, 729
Seward, F. D., & Wang, Z.-R. 1988, ApJ, 332, 199
Tanaka, Y., Inoue, H., & Holt, S. S. 1994, PASJ, 46, L37
Tucker, W. H. 1977, Radiation Processes in Astrophysics (Cambridge: MIT Press)
Wang, Q. D. 1995, ApJ, 453, 783
Wang, Q. D., & Helfand, D. J. 1991, ApJ, 370, 541
Wang, Q. D., Li, Z.-Y., & Begelman, M. C. 1993, Nature, 364, 127